Performance of R/C Bridge Piers under Seismic Loads

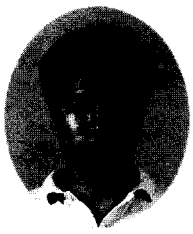

Kang, Hong-Duk* Kang, Young-Jong** Yoon, Young-Soo***

ABSTRACT

A research program was initiated at the University of Colorado at Boulder to develop computational models that can be used for seismic risk assessments. To assess the overall performance of bridge structures including the nonlinear effects of bridge piers, the research focused on two levels of capabilities, i.e. global and local pier levels. A 3-D concrete model was used to evaluate the behavior of individual piers under combined axial, bending, and shear loadings using 3-D finite element analysis. Whereby the response curve reached the peak strength of the R/C column under the constant axial and monotonically increasing lateral loads. Experimental results on reinforced concrete bridge piers, which were obtained at the University of California at San Diego were used to validate the seismic performance of bridge piers at the two levels, global and local.

Keywords : Triaxial Concrete Model, Bridge Column, Fiber Model, Elasto-Plasticity

* Intern-Researcher, Dept. of Civil and Environmental, Korea University, Korea
** KCI Member, Associate Professor, Dept. of Civil and Environmental, Korea University, Korea
*** KCI Member, Associate Professor, Dept. of Civil and Environmental, Korea University, Korea

1. Introduction

The vulnerability of highway bridges to earthquake ground motions was very apparent in a number of major earthquakes, such as the 1971 San Fernando, the 1989 Loma Prieta, and the 1994 North ridge earthquakes in California, and the recent 1995 Hyogoken-Nanbu earthquake[3] in Japan. Bridge structures which were severely damaged in the Hyogoken-Nanbu earthquake were designed with older code provisions, which did not have specific detailing requirements to ensure sufficient ductility of the piers. While most of the catastrophic failures of reinforced concrete bridge piers in that earthquake can be attributed to inadequate confinement or transverse reinforcement, the damage induced in numerous oversized piers is still difficult to understand without detailed engineering analysis. This includes severe bending and crushing failures, as well as brittle diagonal shear failures which took place in many oversized piers.

A research project was carried out at the University of Colorado at Boulder to explain some of the failure phenomena of bridge piers in the Hygoken-Nanbu earthquake. This paper demonstrates the overall response behavior of the flexibility-based fiber model for the column analysis, and a three-dimensional constitutive model for concrete[4], which is designed to capture diffused and localized failure modes under different triaxial load scenarios. To illustrate the performance of these different models with engineering problem of general interest, the nonlinear behavior of a reinforced concrete column tested at the University of California at San Diego[9] was studied from different approaches.

2. Column Description

Two columns tested at the University of California, San Diego[9], were selected for the study which are labeled R-1 and R-3. The columns have the same geometry depicted in Fig. 1 with the material properties summarized in Table 1. Rotations at the two ends of the columns were restrained. A constant axial force of 25402 N (approximately equal to 4.5% Po, the axial strength of the R/C column) was applied, followed by increasing cycles of imposed lateral displacements. The experimental responses are represented by the continuous lines in Fig. 2 and 3. Column R-1 failed primarily in a bending pattern, with horizontal bending cracks appearing first and diagonal shear crack appearing only in the last cycles.

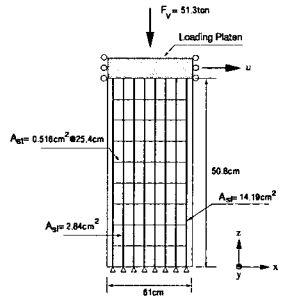

(a)

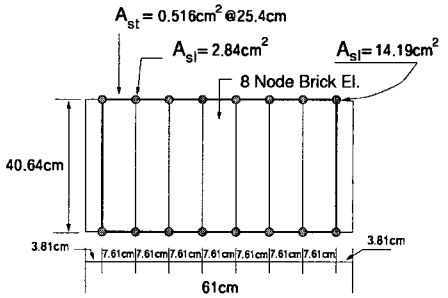

(b)

Fig. 1 (a) Elevation of R/C column.
(b) Cross section of R/C column.

Column R-3 showed a somewhat different behavior where shear cracks formed earlier than in specimen R-1 and strength degradation due to shear-failure dominated the last cycles.

2.1 Fiber Model Study of R/C Columns

A numerical study was conducted to assess the performance of nonlinear frame elements proposed by Spacone et al.[7] in describing the response of bridge piers to large lateral sways. The formulation was based on the force method and assumed constant axial force and linear bending moment along the element. One beam element with five integration points was used for columns R-1 and R-3. Each cross section was discretized into fifteen concrete layers across its depth. No distinction was made in this study between confined and unconfined concrete fibers.

Experimental and numerical predictions are illustrated in Fig. 2 and 3 together. The numerical results for column R-1 showed good agreements with the experimental responses, showing the beam capability to reflect the bending behavior of the structure. The difference in the initial stiffness is probably due to the bond-slip observed in the longitudinal reinforcement at the column ends. It should be noted that the drastic loss of the strength of the column in the final cycles is not captured by the beam element, because the model by Spacone et al.[7] does not account

Table 1 Material properties of R/C columns

Column	Concrete	Axial Steel	Hoop Steel
R-1	f_c'=38MPa	f_y=317MPa	f_y=361MPa
R-2	f_c'=34MPa	f_y=470MPa	f_y=324MPa

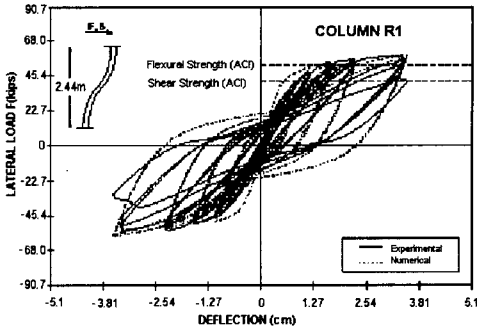

Fig. 2 Cyclic response of column R1.

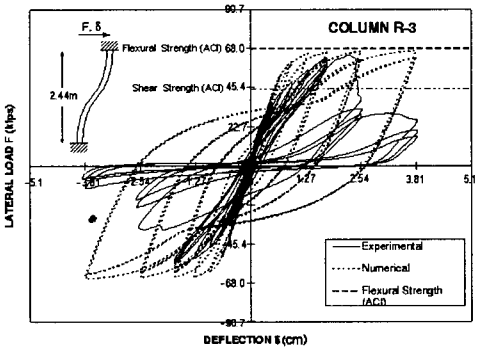

Fig. 3 Cyclic response of column R3.

for shear deformations or shear failure. This discrepancy becomes more evident for column R-3. Shear cracks developed at the early stages of the experiment and strength degradation due to shear failure were evident from displacements smaller than 2.54cm. Since the element neglects the shear behavior of the beam, it cannot describe the shear deformation even though the element does capture the bending and axial behavior of reinforced concrete columns. Fig. 2 and 3 also show the flexural and shear strengths computed according to the ACI code provisions1. While the flexural strength is close to the experimental and numerical results, the shear strength predicted by the ACI code is very conservative and underestimates the observed column strength.

3. Triaxial Concrete Model

The three-dimensional concrete model is based on an elasto-plastic constitutive formulation in which the initial yield surface and the failure envelope bound the hardening regime of concrete in tension and compression, respectively, as shown in Fig. 6. After the stress path reaches the failure envelope, the concrete model exhibits strain softening depicted in Fig. 7 under progressive straining in triaxial tension, and perfect plasticity under highly confined compression. Thereby, the concrete model captures both hardening and softening in compression and tension as indicated in the uniaxial stress-strain curves in Fig. 4. A non-associated flow rule plays a significant role in characterizing plastic dilatation in order to assure realistic predictions of inelastic volume changes at different confinement levels. The main features of the concrete model and its distinction from other existing models are briefly summarized below.

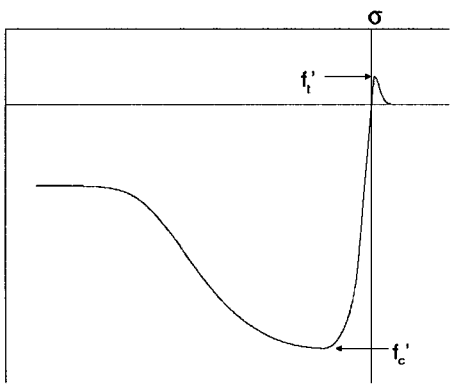

Fig. 4 Uniaxial stress-strain behavior.

3.1 Elasto-Plastic Formulation

Based on standard flow theory of elasto-plasticity, the strain rate can be decomposed additively into an elastic component and aplastic components, $\dot{\boldsymbol{\varepsilon}} = \dot{\boldsymbol{\varepsilon}}_e + \dot{\boldsymbol{\varepsilon}}_p$ in the case of infinitesimal deformations. The elastic strain rate is related to the stress rate by Hooke's law:

$$\dot{\boldsymbol{\sigma}} = \boldsymbol{E} : \dot{\boldsymbol{\varepsilon}}_e = \boldsymbol{E} : (\dot{\boldsymbol{\varepsilon}} - \dot{\boldsymbol{\varepsilon}}_p) \quad (1)$$

where $\mathbf{E} = \Lambda \boldsymbol{\delta} \otimes \boldsymbol{\delta} + 2G\mathbf{I}_4$ denotes the isotropic elasticity tensor. Assuming that there is no elastic damage, the elastic properties remain constant during the entire plastic deformation process. The elastic range is delimited by the plastic yield condition:

$$F(\boldsymbol{\sigma}, q_h, q_s) = 0 \quad (2)$$

where the size and shape of which depend on two internal variables q_h and q_s for describing the increase of strength due to hardening and the degradation of strength due to tensile softening, respectively. In the case of plastic loading, the direction of the plastic strain rate is governed by the non-associated flow rule:

$$\dot{\boldsymbol{\varepsilon}}^p = \dot{\lambda} \frac{\partial Q}{\partial \boldsymbol{\sigma}} = \dot{\lambda} \mathbf{m} \quad (3)$$

where Q denotes the plastic potential and $\dot{\lambda}$ the plastic multiplier. The latter is determined with the help of the plastic consistency condition, $F_{n+1}(\Delta\lambda) = 0$, which assures that the constitutive behavior under persistent plastic deformations is consistent within the finite time interval

$$\Delta t = t_{n+1} - t_n .$$

3.2 Yield Function

The curvilinear loading surface $F(\sigma, q_h, q_s) = 0$ maintains C^1-continuity except for the apex in equitriaxial tension. The deviatoric sections of the triaxial failure envelope in Fig. 5 have a triangular shape in tension and low confined compression which gradually transforms into a circular shape under increasing hydrostatic pressure (see sections 1-2-3 in Fig. 5).

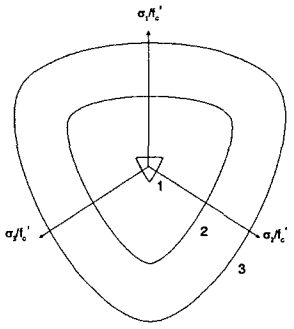

Fig. 5 Deviatoric sections of triaxial failure envelope.

3.2.1 Strain Hardening

In the hardening regime, the plastic yield condition

$$F(\xi,\rho,\theta,k) = \rho r(\theta,e) - \rho_1\left\{\left(\frac{\xi-\xi_0}{\xi_1-\xi_0}\right)^{\alpha} + \left[\left(\frac{\xi-\xi_1}{\xi_0-\xi_1}\right)^{\beta} - 1\right]\right\} = 0 \tag{4}$$

is a function of the Haigh-Westergaard stress coordinates, resulting in the three stress invariants, $\xi = I_1/\sqrt{3}$, $\rho = \sqrt{2J_2}$, $\theta = \frac{1}{3}\cos^{-1}\left(\frac{3\sqrt{3}}{2}\frac{J_3}{\sqrt{J_2^3}}\right)$.

Hardening is controlled by the normalized hardening variable $k = k(q_h, \xi)$ which varies between $0 \le k \le 1$ where q_h corresponds to the equivalent plstic strain and ξ introduces the effect of hydrostatic stress on the nonlinear hardening response. The exponent α accounts for the pressure-sensitivity of the triaxial concrete strength(i.e., $\alpha = 0.5$ shows a failure surface in the form of a triple symmetric paraboloid)

Strain hardening is governed by the exponent $\beta(k)$ in the loading function Eqn. (4) where

$$\beta = 0.25\frac{1-k^2}{1-k_0^2} \tag{5}$$

k_o= initial value of k

is a function of the hardening measure $k = k(q_h, \xi)$ where k is defined as

$$k = \frac{2}{h_D}(1-k_0)(\sqrt{2h_D\varepsilon_p} - \varepsilon_p) + k_0$$
$$h_D = A_h\left(\frac{\xi}{f_c'}\right)^2 + B_h\left(\frac{\xi}{f_c'}\right) + C_h \tag{6}$$

According to Eqn.(5), the exponent $\beta(k)$ in the hardening term of the yield function varies from 0.25 to 0 when $k_o \le k \le 0$. When $\beta = 0$, the compression cap fully opens up and

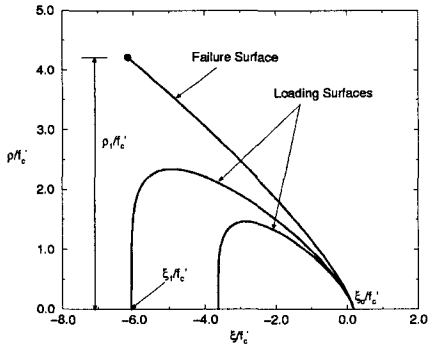

Fig. 6 Strain hardening meridians.

the compressive meridian (corresponding to $\theta = 60^{\circ}$) of the loading surface reaches the failure envelope, as shown in Fig. 6. Therefore, the compressive meridian of the failure surface passes through the point of uniaxial compression.

3.2.2 Strain Softening

When the stress path reaches the failure surface, $\beta \rightarrow 0$ as indicated in Eqn. (5) and the hardening term becomes inactive. Progressive straining in triaxial tension mobilizes softening of the yield condition in Eqn. (7) which is augmented by the normalized decohesion variable $1 \geq c(q_s, \xi) \geq 0$:

$$F(\xi, \rho, \theta, c) = \rho r(\theta, e) - \rho_1 \{ (\frac{\xi - \xi_0}{\xi_1 - \xi_0})^{\alpha} - (1-c)(\frac{\xi_0}{\xi_0 - \xi_1})^{\alpha} (\frac{\xi_c - \xi}{\xi_c})^2 \} = 0 \quad (7)$$

The above equation is valid for $\xi \geq \xi_c$. Note that $\xi_c = -T\xi_o$ locates the transition point of brittle/ductile fracture below which softening takes place. For $\xi \leq \xi_c$, the yield surface coincides with the failure envelope and the behavior of the material is almost perfectly plastic in that region. The change of the loading surface due to strain softening is illustrated in Fig. 7 where the strain softening parameter $c = c(q_s, \xi)$ controls tensile degradation and is a function of the equivalent tensile fracture strain

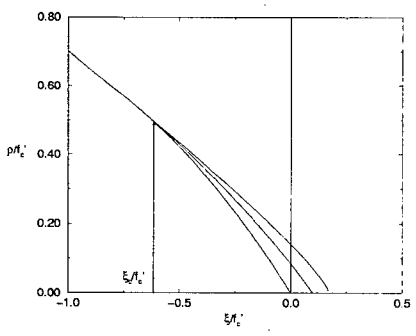

Fig. 7 Strain softening meridians.

$$c = \frac{1.0}{\exp[\delta(u_f / s_f)^2]} \quad (8)$$

where $u_f = \varepsilon_f l_c$

$\varepsilon_f = \int \dot{\lambda} \| \mathbf{m}_t \|_2 dt$

$s_D = A_s(\xi - B_s f_c')^4 + 1.0$

A_s, B_s = constants

which is a function of the equivalent tensile fracture strain. The internal softening variable is activated by the equivalent tensile fracture strain, q_s, from the time at which the stress path reaches the failure envelope. In the equation, $\boldsymbol{m}_t$ extracts only tensile components from the gradient of the plastic potential $\boldsymbol{m}$, l_c denotes the characteristic length for fracture energy-based strain softening, and $S_D(\xi)$ accounts for the influence of the confinement pressure on the slope of the softening branch. The value of the strain softening variable $c(q_s, \xi)$ varies according to the state of decohesion from zero to one($1 \leq c(q_s, \xi) \leq 0$)

3.3 Plastic potential

A non-associated flow rule is adopted for realistic predictions of concrete dilatation at different levels of confinement. The plastic potential has the same structure as Eqns. (4) and (7) but with the exponent α replaced by $\bar{\alpha}$. Experimental data on concrete materials indicate that $0 < \bar{\alpha} < \alpha$.

4. Performance of Triaxial Concrete Model in Shear

The constitutive model presented in the previous section has been calibrated with the data of conventional triaxial compression tests[2] with confinement pressures of p=0, 0.69, 3.45 *MPa*, respectively. The parameter values are summarized in Table 2.

Table 2 Material parameters.

f_c' MPa	ξ_0 MPa	α	S	A_h	B_h
34.0	6.2	0.77	0.7	-.000283	-0.00572
C_h	T	A_s	B_s	δ	$\bar{\alpha}$
.000424	8.2	.000222	.65818	$10^{a,3}$	0.23

The performance of the concrete model under pure and simple shear were studied recently with a particular focus on the difference of shear failure under different levels of confinement8. Fig. 8 shows the shear response which leads to tensile cracking at $\theta = 45^o$ according to the maximum stress hypothesis of Rankine which characterizes failure in "*pure shear*".

The failure mode is illustrated in Fig. 12(a). Pure shear is a stress-controlled experiment in which only the shear stress increases $\dot{\tau}_{xz} > 0$, while all other stress components remain zero. Thus, the failure mode is very brittle due to the formation of a diagonal tensile crack according to $f_t' = 3.8MPa$. In contrast, simple shear is a fully strain-controlled experiment in which only the shear strain $\dot{\gamma}_{xz} > 0$ increases, while all other strain components remain zero. Thus, the simple shear response in Fig. 9 exhibits strength and ductility values which

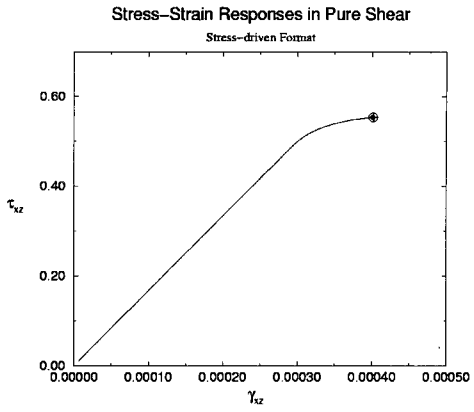

Fig. 8 Pure shear response

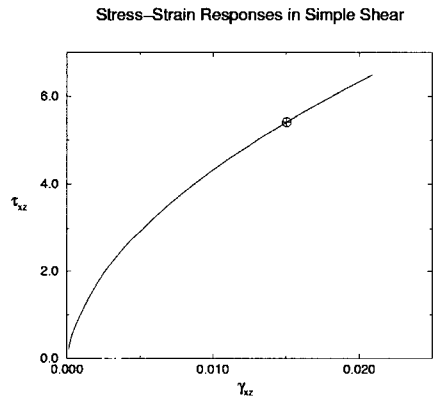

Fig. 9 Simple shear response

exceed tenfold than those under pure shear in Fig. 8 due to the confinement effect induced by the kinematic constraint of zero normal strain. The corresponding failure mode shown in Fig. 12(b) demonstrates the significant difference between pure shear and simple shear. The latter is governed by compression-slip at the point of localized failure denoted by the symbol ⊕ which takes place in the ascending branch of the response curve of Fig. 9. The large discrepancy of strength and ductility in pure and simple shear reflect the important difference in shear behavior of reinforced concrete columns with and without confinement due to high quan-

tities of longitudinal and transverse reinforcing steels.

The shear behavior in a R/C column lies between the two extremes of no confinement in pure shear and full confinement in simple shear. The subsequent study is an attempt to provide additional insight into the behavior of the shear critical section at mid-height of the R/C column. Thereby a plain concrete brick element is subjected to mixed compression-shear boundary conditions which emulate constant axial load and monotonically increasing lateral shear force without constraining out-of-plane deformations. The response of this mixed compression-shear test is shown in Fig. 10. This indicates an increase of shear strength of 100 % beyond the shear strength in pure shear. The plot also shows that the localization, indicated by the symbol ⊕ in Fig. 10 occurs slightly earlier than the loss of stability marked by the symbol •. The localized failure mode of this experiment is also depicted in Fig. 12(c) which shows a little increase of the dominant slip angle from 74° to 78° between the normal vector and the governing slip direction when compared to the fully confined case of simple shear.

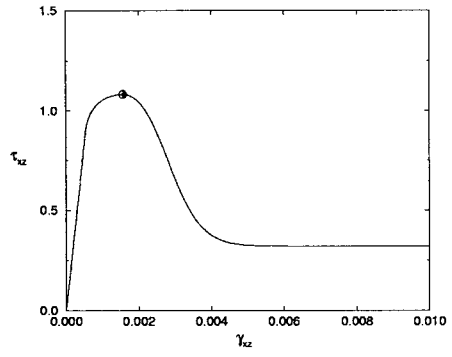

Fig. 10 Shear-compression response of plain concrete.

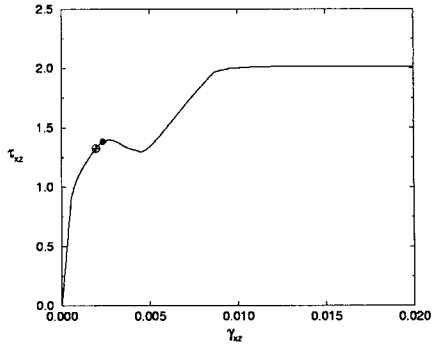

Fig. 11 Shear-compression response of reinforced concrete

In a final attempt to emulate the behavior of the R/C column R-3 which has been discussed earlier, the shear-compression experiment on plain concrete is expanded to include longitudinal and transverse reinforcement at the boundaries of the brick element. The response of the reinforced concrete element is shown in Fig. 11 that illustrates the effect of axial and transverse reinforcing steels over the response of plain concrete. Both tests impose a monotonically increasing shear strain $\dot{\gamma}_{xz} > 0$, while $\varepsilon_x \neq 0, \varepsilon_z \neq 0$ and $\varepsilon_y \neq 0$. It is important to note that the shear strain reading at concrete failure of the reinforced specimen indicates an increased ductility of 80 % and by 650 % when compared to plain concrete (Fig. 10) and to the pure shear response (Fig. 8), respectively. The additional confinement of the axial and transverse reinforcements also increases the shear strength of the reinforced concrete specimen up to $\tau_{xz}^{max} = 14.1 MPa$ (i.e. by another 100 %) beyond the shear strength of the plain concrete specimen. This corresponds to the yield capacity of the transverse stirrups. Up to this stage, the shear response exhibits the typical tension stiffening effect of reinforced concrete with a hump in the

ascending branch when the tensile concrete strength is being exhausted. In other terms, longitudinal and transverse steels regularize the shear behavior and drive the shear response of the reinforced concrete specimen

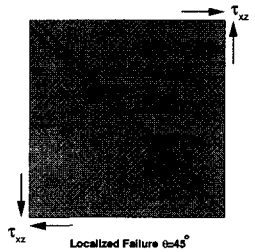

(a) Pure shear

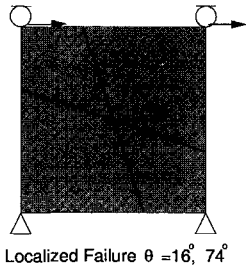

(b) Simple shear

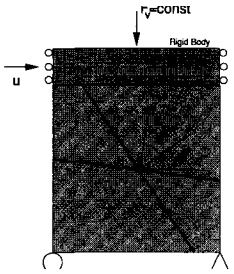

(c) Plain concrete

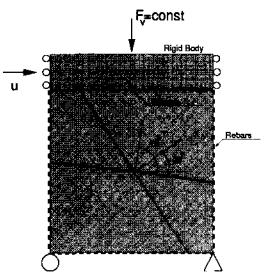

(d) R/C panel in shear-compression

Fig. 12 Different shear modes of failure of triaxial concrete model

to the flat plateau as depicted in Fig. 11. Pre-peak response in Fig. 11 indicates localized failure, however it is being regularized by the axial and transverse reinforcement bars along the slip planes as illustrated in Fig. 12(d).

5. 3-D Analysis of Bridge Columns

In the final study, the reinforced concrete bridge column tested by Xiao et al.[9] was analyzed with the new concrete model. The cross section of the column, which is designated as R-1 in the report by Xiao et al., was idealized for numerical studies as shown in Fig. 1. The rectangular column with L=2440 mm was subjected to lateral displacement cycles with the top and bottom being fixed from rotation, while the axial load of $F_V = 25402\ N$ was fixed constant during the cyclic load program. The longitudinal reinforcement ratio was $\rho_z = 2.5\%$ while the transverse stirrups were #2 hoops at h=127 mm. spacing. Both the longitudinal and transverse reinforcement was made of Grade 40 steel. The actual yield strength of the longitudinal steel was, however, f_y=317 *MPa*, while that of the transverse steel was f_y=359 *MPa*. The concrete had a compressive strength of $f_c' = 38\ MPa$ at 28 days. The experimental failure mode of this column was characterized as *"flexural shear"* in the original experimental report as it reached the theoretical flexural strength in the test, but the final rupture in the post-peak regime was governed by shear as shown in Fig. 2.

Results of the three-dimensional analysis are described below. In the finite element mesh depicted in Fig. 13, the reinforcing steel

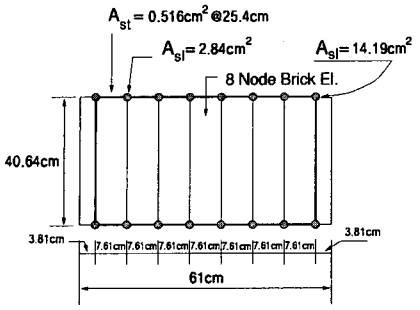

Fig. 13 Finite element discretization of cross-section

is modeled with bar elements that are fully bonded to the hexahedral concrete elements. Thereby, the area of the longitudinal rebars was weighted differently with more steel being concentrated at the outside fibers of the cross section than in the interior. Since other material data were not available besides the uniaxial compressive strength of concrete, the parameter values of the concrete model shown in Table 2 were used in this analysis except for $f_c^{'} = 38\ MPa$ and $\xi_o = 6.9\ MPa$.

In the three-dimensional simulation, the behavior of the reinforced concrete column is analyzed under a monotonically increasing lateral displacement and constant axial load. The numerical result is compared to the experimental data in Fig. 14 and the deformed shape of the column is depicted in Fig. 17. The experimental data shown in the

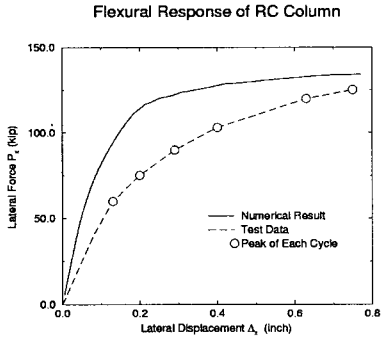

Fig. 14. R/C column loaded in compression-shear

Fig. represent the peak load reached in the first cycle of each ductility level. While the finite element model captures the strength of the reinforced concrete column, the numerical result exhibits somewhat higher stiffness than the experimental. The discrepancy between the experimental and numerical results could be caused by several factors such as (i) the difference between the monotonically increasing lateral displacement analysis and the cyclic displacement reversals of the experimental load program and (ii) the bond slip of the longitudinal steel anchors that was ignored in the analysis. The fiber strains in the longitudinal reinforcement bar at the top and bottom of cross-sections of the column as depicted in Fig. 15(a) and (b) do compare

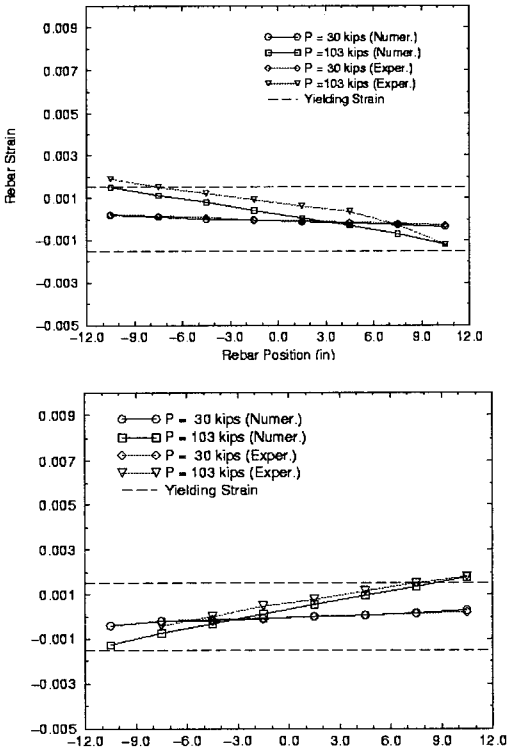

Fig. 15 Strain distributions of longitudinal rebars along cross sections of (a) top, and (b) bottom of the column.

well with the test data indicating a fairly planar distribution of longitudinal fiber strains except for the increase at the compressive toe of the cross-section when the lateral load reaches $P = 23154\ N$. The shear deformation predictions also compare quite well with the experimental measurements in three segments along the height of the column as shown in Fig. 16. However, the numerical results indicate that the shear deformations at the base are underestimated near the maximum lateral load $P = 26976\ N$ by the analysis which indicates again towards additional bond slip effects at the anchorage of the longitudinal reinforcement that was not included in the analysis.

In summary, the finite element model captures the flexural response of the column rather well since it accounts fully for the triaxial confinement effect of the transverse reinforcement. However, the analysis has not gone beyond the peak point due to the nature of highly induced nonlinearity in the complex column. This remains to be studied in the near future.

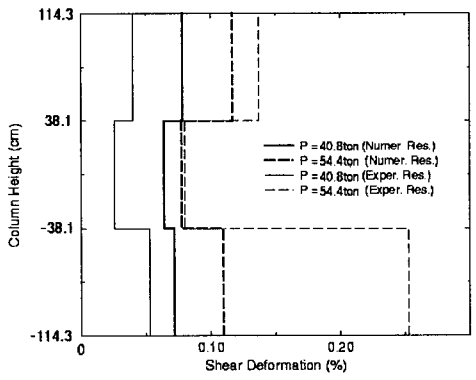

Fig. 16 Distribution of shear deformations in tree (top, mid. and bottom) different sections of the column, and comparison to experimental results.

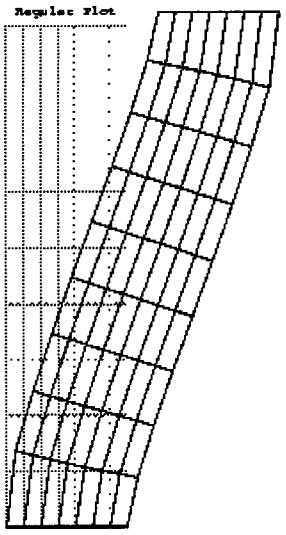

Fig. 17 Deformed shape of column under constant compression and increasing lateral loadings

6. Conclusions

The results of a beam-column analysis showed the capabilities and limitations of the 1-D fiber formulation when the R/C column is failing in shear.

At the other extreme of one and three-dimensional analyses, a triaxial concrete model was introduced for the analysis of reinforced concrete bridge piers. The model accounts for the effect of lateral confinement on the behavior of concrete in terms of stiffness, strength and ductility. The triaxial concrete model was subjected to a number of shear experiments which illustrates the exceptional influence of confinement.

Subsequently, the triaxial concrete model was applied to the analysis of a reinforced concrete column which had been tested at the University of California at San Diego. The numerical results showed a good correlation with experimental ones. However, further

studies are needed to analyze more precisely selected bridge piers that were severely damaged in the Hyogoken-Nanbu earthquake.

Acknowledgment

The writers gratefully acknowledge that the study presented in this paper is sponsored by the Earthquake Hazard Mitigation Program of the National Science Foundation under Grant No. CMS-9622940. However, opinions expressed in this paper are of the writers and do not necessarily reflect those of the sponsor.

References

1. ACI 318-95, Building Code Requirements for Structural Concrete and Commentary, American Concrete Institute, Committee 318, 1995.
2. Hurlbut, B.J., Experimental and Computational Investigation of Strain-Softening in Concrete, *M.S. Thesis*, University of Colorado, Boulder, 1985.
3. EERI., The Hyogo-Ken Nanbu Earthquake - January 17, 1995, *Report No. 95-04*, Earthquake Engineering Research Institute, Oakland, 1995.
4. Kang, H. and Willam, K. (1999), *Localization Characteristics of Triaxial Concrete Model*, ASCE *J. Eng. Mech.*, Vol. 125, pp. 941-950.
5. Reinhardt, H. W., and Walraven, J. C., Cracks in Concrete Subject to Shear, *J. Struct Div.* ASCE, 108 (ST1), 207 - 224, 1982.
6. Seismic Advisory Board., The Continuing Challenge The Northridge Earthquake of January 17, 1994, *Report to the Director*, California Department of Transportation, Sacramento, June 1994.
7. Spacone, E., Filippou, F.C., and Taucer, F.F., Fiber Beam-Column Model for Nonlinear Analysis of R/C Frames.-I. Formulation. *Earthquake Engineering and Structural Dynamics*, 25 (7), 711-725, 1996.
8. Willam, K., Kang, H., Shing, B. and Spacone, E., Analysis of Shear Failure in Concrete Materials, Proc. of IUTAM Symposium *Material Instabilities in Solid*, R. De Borst and E. Van Der Giessen eds., John Wiley & Sons, Delft, June 9-13, 1997, Chapter 3, pp 27-39.
9. Xiao, Y., M.J. Nigel Priestley, and Frieder Seible., Steel Jacket Retrofit for Enhancing Shear Strength of Short Rectangular Reinforced Concrete Columns, *Report No. SSRP-92/07*, University of California, San Diego, July 1993.